

Mars Methane Sources in Northwestern Gale Crater Inferred from Back-Trajectory Modeling

Yangcheng Luo¹, Michael A Mischna², John C. Lin³, Benjamin Fasoli³, Xiang Cai⁴, and Yuk L. Yung¹

¹California Institute of Technology

²Jet Propulsion Laboratory

³University of Utah

⁴Santiago High School

November 22, 2022

Abstract

During its five years of operation as of 2017, the Sample Analysis at Mars (SAM) Tunable Laser Spectrometer (TLS) on board the Curiosity rover has detected six methane spikes above a low background abundance in Gale crater. The methane spikes are likely sourced by nearby emission from the surface. Here we use inverse Lagrangian modeling techniques to identify upstream emission regions on the Martian surface for these methane spikes at unprecedented spatial resolutions. Inside Gale crater, the northwestern crater floor casts the strongest influence on the detections. Outside Gale crater, the upstream regions extend towards the north. The contrasting results from two consecutive TLS methane measurements point to an active emission site to the west and the southwest of the Curiosity rover on the northwestern crater floor. The observed spike magnitude and frequency also favor emission sites on the northwestern crater floor, unless there are fast methane removal mechanisms at work, or either the TLS methane spikes or the Trace Gas Orbiter (TGO) non-detections can not be trusted.

1 **Mars Methane Sources in Northwestern Gale Crater Inferred from Back-Trajectory**

2 **Modeling**

3 **Enter authors here: Y. Luo¹, M. A. Mischna², J. C. Lin³, B. Fasoli³, X. Cai⁴, and Y. L.**
4 **Yung^{1,2}**

5 ¹Division of Geological and Planetary Sciences, California Institute of Technology, Pasadena,
6 CA 91125, USA

7 ²Jet Propulsion Laboratory, California Institute of Technology, Pasadena, CA 91109, USA

8 ³Department of Atmospheric Sciences, University of Utah, Salt Lake City, UT 84112, USA

9 ⁴Santiago High School, Corona, CA 92881, USA

10 Corresponding author: Y. Luo (yc.luo@caltech.edu)

11 **Key Points:**

- 12 • Back-trajectory analyses are performed for the methane spikes detected by the Mars
13 Science Laboratory at Gale crater.
- 14 • Upstream emission regions are mapped out at unprecedented spatial resolutions.
- 15 • Provided a 330-year methane lifetime, the emission site(s) must be located next to the
16 *Curiosity* rover in northwestern Gale crater.

17

18 **Abstract**

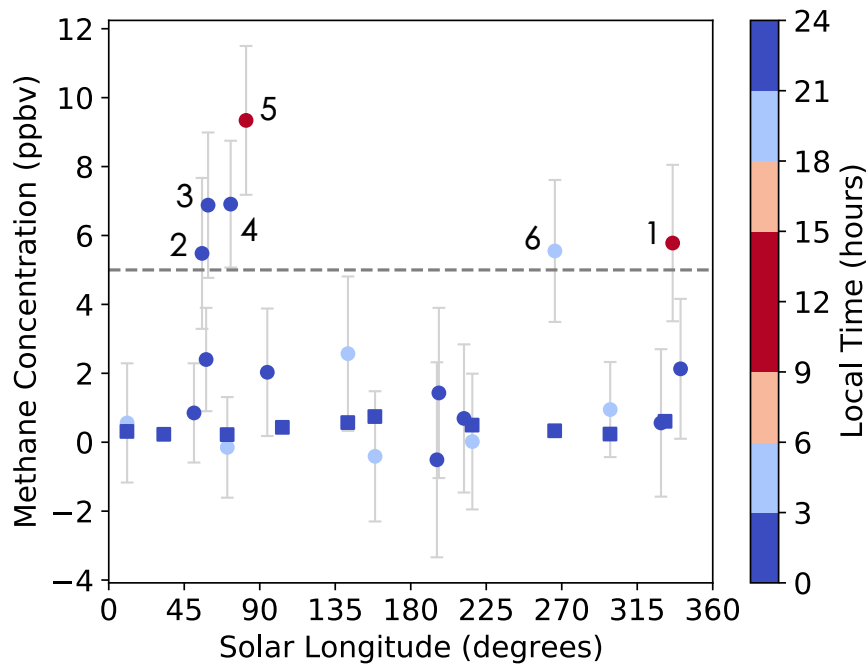
19 During its five years of operation as of 2017, the Sample Analysis at Mars (SAM) Tunable Laser
20 Spectrometer (TLS) on board the *Curiosity* rover has detected six methane spikes above a low
21 background abundance in Gale crater. The methane spikes are likely sourced by nearby emission
22 from the surface. Here we use inverse Lagrangian modeling techniques to identify upstream
23 emission regions on the Martian surface for these methane spikes at unprecedented spatial
24 resolutions. Inside Gale crater, the northwestern crater floor casts the strongest influence on the
25 detections. Outside Gale crater, the upstream regions extend towards the north. The contrasting
26 results from two consecutive TLS methane measurements point to an active emission site to the
27 west and the southwest of the *Curiosity* rover on the northwestern crater floor. The observed
28 spike magnitude and frequency also favor emission sites on the northwestern crater floor, unless
29 there are fast methane removal mechanisms at work, or either the TLS methane spikes or the
30 Trace Gas Orbiter (TGO) non-detections can not be trusted.

31 **1 Introduction**

32 Almost all of the methane in the present-day Earth's atmosphere can be traced back to
33 biological origins (Cicerone and Oremland, 1988). Extending this observation to Mars, this
34 would suggest that the presence of methane in the Martian atmosphere could be a biosignature
35 on this seemingly lifeless planet (Yung et al., 2018). Alternative, abiotic methane production
36 mechanisms on Mars invoke past or present geological activity (reviewed in Oehler and Etiope,
37 2017) such as serpentinization (Oze and Sharma, 2005), which indicates the presence of liquid
38 water, an indispensable ingredient for life. Abundant methane in the ancient Martian atmosphere
39 could also provide a solution to the conflict between the Faint Young Sun and a warm surface
40 suggested by fluvial and lacustrine features on Mars (e.g., Kite et al., 2017).

41 In the past two decades, the significance of methane in the Martian atmosphere has
42 motivated a number of remote sensing observations aimed at retrieving the methane abundance
43 in the Martian atmosphere and mapping out its spatial distribution. They reported inconsistent
44 and highly variable methane concentrations (Krasnopolsky et al., 2004; Formisano et al., 2004;
45 Geminale et al., 2008; Mumma et al., 2009; Fonti and Marzo, 2010; Krasnopolsky, 2012; Aoki et
46 al., 2018; Giuranna et al., 2019). To overcome the technical challenges faced by remote sensing
47 observations, the Tunable Laser Spectrometer (TLS; Mahaffy et al., 2012) on board the *Curiosity*
48 rover was sent to Gale crater to make *in situ* measurements. During 4.6 years of operation as of
49 May 2017, twenty direct-ingest measurements and ten enrichment measurements (refer to
50 Webster et al. (2015) and Webster et al. (2018) for the descriptions for the two measurement
51 types) revealed a baseline level of ~ 0.41 parts-per-billion-by-volume (ppbv), with episodic
52 spikes up to ~ 10 ppbv (Webster et al., 2018) as summarized in Fig. 1. These spikes have been
53 interpreted as discrete methane emission events (Webster et al., 2015, 2018). Notably, a methane
54 spike with an unprecedentedly high magnitude, 20.5 ppbv, was announced very recently in Webster
55 et al. (2021). It was the first time that a methane spike had been detected in an enrichment
56 measurement, with a low signal-to-noise ratio of ~ 5 , thus adding to the credibility of the previous
57 methane spikes. Concurrently, the ExoMars Trace Gas Orbiter (TGO) has made solar occultation
58 measurements for the methane concentration in the mid- to high-altitudes. However, it has
59 reported stringent upper limits down to 0.02 ppbv (Korablev et al., 2019; Knutsen et al., 2021;
60 Montmessin et al., 2021). Assuming methane is a long-lived species with a 330-year lifetime as
61 indicated by standard photochemical models (Lefèvre and Forget, 2009), it will be uniformly
62 mixed throughout the Martian atmosphere, so TGO's stringent upper limits obtained in a few
63 detections has been interpreted as the upper limit for methane concentration in the entire

64 atmosphere, which is then contradictory to TLS’s significantly more elevated ~ 0.41 ppbv
 65 background level. Some mechanisms have been proposed to reconcile this inconsistency. TLS
 66 performed all its measurements in the near-surface planetary boundary layer (PBL), and
 67 methane, if released from the surface, could accumulate in the shallow nighttime PBL (Moores et
 68 al., 2019a, 2019b). Some speculative fast removal mechanisms that can possibly cause temporal
 69 and spatial inhomogeneity of methane concentration have also been proposed (Gough et al.,
 70 2010; Knak Jensen et al., 2014; Hu et al., 2016), which may also potentially reconcile the
 71 inconsistency between the TLS and the TGO results. In this study, we first accept both the results
 72 from TLS and TGO, and investigate the circumstances in which their discrepancies can be
 73 reconciled. We will later re-evaluate the probability of these circumstances.



74

75 **Figure 1. TLS methane signals versus Mars season and local time.** The six data points above
 76 the horizontal dashed line at 5 ppbv are regarded as the “methane spikes” with their indices
 77 labelled next to them. The twenty-four data points below the dashed line are regarded as the

78 background abundance. All the measurements were made in the nighttime except Spikes 1 and 5,
79 which were measured in the early afternoon. Direct-ingest measurements are shown in circles.
80 Enrichment measurements are shown in squares. Colors show the local time of ingestions. Error
81 bars show ± 1 standard error of the mean for each measurement. Adapted from Webster et al.
82 (2018).

83 Assuming the existence of methane on Mars is real, its origin will have great implications
84 for geology and astrobiology. The identification of the methane origin requires that we first find
85 the surface emission sites, results from which can inform future missions of high priority landing
86 sites and enable them to directly probe the methane source. The results can also guide orbiting
87 instruments to better focus their methane observation strategies.

88 Inferring the locations of methane emission sites requires correct modeling of complex
89 atmospheric transport processes. An early attempt to do so involved using a diffusion model to
90 represent the spread of observed methane plumes (Mumma et al., 2009), which was shown to be
91 oversimplified by addressing the importance of advection by bulk wind (Mischna et al., 2011).
92 More recently, the Global Environmental Multiscale (GEM)-Mars general circulation model
93 (GCM) was used to simulate methane transport and then a statistical approach based on the idea
94 of simultaneous satisfaction of multiple observational constraints was used for methane source
95 localization (Giuranna et al., 2019). Results suggested an emission region to the east of Gale
96 crater for TLS's first methane spike (Spike 1 in Fig. 1). Later, the Mars Regional Atmospheric
97 Modeling System (MRAMS) model was used to simulate the transport and dispersion of
98 methane plumes emitted from ten selected source regions around Gale crater (Pla-García et al.,
99 2019). Substantial dilution during tracer transport was observed, which demonstrates the
100 importance of incorporating turbulent dispersion into tracer transport modeling. Among all the

101 ten emission region candidates, the region to the northwest of the crater was favored, different
102 from previous findings (e.g., Giuranna et al., 2019).

103 The aforementioned emission site localization studies all adopted a forward Eulerian
104 approach, in which the model integrates three-dimensional tracer fields forward in time and
105 quantifies how much tracer released at a specific emission location and time can ultimately reach
106 the detector. However, this “trial-and-error” approach is computationally inefficient, as most of
107 the released particles do not reach the detector, so usually only a small number of putative
108 emission sites are selected and studied in depth (e.g., Pla-García et al., 2019). Meanwhile, the
109 spatial resolution of emission regions is limited by the size of GCM grid boxes, making it
110 difficult to differentiate emission sites within Gale crater (e.g., Giuranna et al., 2019).

111 In this work, we adopt an inverse Lagrangian approach (Lin et al., 2003, 2012) to
112 overcome the challenges faced by forward Eulerian emission site localization techniques. The
113 inverse Lagrangian approach is also known as back-trajectory analysis and is widely used in the
114 environmental science community to map out upstream emission regions (e.g., Lin et al., 2003;
115 Gerbig et al., 2003; Lin et al., 2004; Kort et al., 2008; Macatangay et al., 2008; Mallia et al.,
116 2015). An ensemble of computational particles, representing air parcels, is released from the
117 detector at the time of detection and is transported backwards in time. The particles’ transport
118 pathways are determined by the bulk wind, and the particles are dispersed by parameterized
119 subgrid-scale turbulence. The locations where backward-travelling particles are found within the
120 PBL and hence are potentially affected by surface emission are identified as potential upstream
121 emission regions. The quantitative linkage between measured atmospheric mole fraction at the
122 detector and upstream surface fluxes is established via the number density of particles at an
123 upstream location (Lin et al., 2003; Fasoli et al., 2018). A single inverse Lagrangian simulation

124 can quantify the influence of all upstream emission regions on a detection, and the spatial
125 resolution of emission regions is not limited by the GCM resolution. As such, high-resolution
126 maps of all upstream emission regions can be produced, which is critical for the search for
127 emission sites within and around the small, 154-km wide, Gale crater.

128 **2 Methods**

129 2.1 GCM wind simulations

130 Since global, high-quality wind observations on Mars have been lacking to date,
131 we use MarsWRF, a GCM of the Martian atmosphere, to simulate the wind fields
132 necessary for inverse Lagrangian modeling. MarsWRF is derived from the terrestrial
133 WRF model and is a Mars-specific implementation of PlanetWRF (Christensen et al.,
134 2001). MarsWRF is a finite-difference grid-point model projected onto an Arakawa-C
135 grid with user-defined horizontal and vertical resolutions. The vertical grid follows a
136 modified-sigma (terrain-following) coordinate from the surface to ~80 km altitude. The
137 total present-day atmospheric CO₂ budget is tuned to fit the Viking Lander annual
138 pressure curves (~6.1 mbar), and both surface albedo and thermal inertia are matched to
139 Mars Global Surveyor Thermal Emission Spectrometer (MGS-TES) observations
140 (Christensen et al., 2001; Putzig et al., 2005), while a Mars Orbiter Laser Altimeter
141 (MOLA) topography base map is employed and scaled to the chosen model resolution.

142 Multiple studies in the past have validated MarsWRF to the maximum possible
143 extent through comparison of its behavior against data from the *Mars Global Surveyor*
144 Thermal Emission Spectrometer (Lee et al., 2011; Toigo et al., 2012; Guzewich et al.,
145 2013, 2014), the *Mars Reconnaissance Orbiter* Mars Climate Sounder (Guzewich et al.,

146 2013), and the weather stations on board *Curiosity* (Fonseca et al., 2018; Newman et al.,
147 2017) and *InSight* (Newman et al., 2020), showing MarsWRF reproduces observed
148 atmospheric pressure, atmospheric and ground temperature, near-surface wind speeds and
149 wind directions reasonably well.

150 MarsWRF permits multiple embedded “nests” with increasing spatial resolutions
151 in a single model run. This allows atmospheric circulations influenced by small-scale
152 topographic features to be fully resolved in a simulation while the simulation also covers
153 the entire globe. In this study, we run MarsWRF at increasing horizontal resolutions
154 around Gale crater. The final model consists of four nested levels, each scaled up in
155 resolution (spatial and temporal) by a factor of three. Level 1 provides global coverage
156 with a horizontal resolution of $2^\circ \times 2^\circ$ and a 60-second timestep. Level 2 encompasses an
157 $80^\circ \times 80^\circ$ domain with a horizontal resolution of $0.67^\circ \times 0.67^\circ$ and a 20-second timestep.
158 Level 3 encompasses a $26.67^\circ \times 26.67^\circ$ domain with a horizontal resolution of
159 $0.222^\circ \times 0.222^\circ$ and a 6.67-second timestep. Level 4 encompasses an $8.89^\circ \times 8.89^\circ$ domain
160 with a horizontal resolution of $0.074^\circ \times 0.074^\circ$ (4.4 km \times 4.4 km) and a 2.22-second
161 timestep (Fig. S1), which fully resolves the crater circulation. Two-way boundary
162 conditions link a nested domain with its “parent”, with information being passed both up
163 and down between parent and child domains. A description of this process may be found
164 in Richardson et al. (2007). In order to speed up the simulations, we performed test
165 simulations in advance to determine the duration of MarsWRF simulations on each

166 nesting level. A higher-level nesting is no longer necessary after 99% of the initially
167 released backward-traveling particles have left the domain of that nesting level.

168 Given the lack of a global coverage of high-quality wind observations, it is
169 impossible to reproduce precise “real” atmospheric circulations on spatial scales smaller
170 than tens of kilometers, as stochastic weather events can significantly impact wind speed
171 and even direction. As a result, at this stage, we do not intend to reproduce the “real”
172 winds. Instead, we aim to produce “mean” winds that are representative of their
173 respective seasons and time of day. For each TLS measurement, we repeat MarsWRF
174 simulations for the corresponding Mars year five times, each time starting from a
175 different initial condition. For each Mars year, the different rounds of GCM simulations
176 are all driven by the same seasonally representative dust loadings. They show slight
177 variations in year-to-year conditions as a consequence of stochastic variability in the
178 weather. The variance in results across the five times of simulation is, however, small.

179 On short timescales (<1 week), it is not anticipated there will be a significant
180 change in the mean atmospheric conditions on Mars, so for each of the five rounds of
181 wind simulations, we treat the sol of measurement, and one, two, three sols before and
182 after the measurement as equally representative of the circulation pattern at the time of
183 the TLS measurement, and release particles at the time of day of each measurement on all
184 of the seven sols. In this way, we form an ensemble of thirty-five back-trajectory
185 simulations for each investigated TLS measurement, and the following analysis is all

186 based on the average footprints of these thirty-five simulations. This ensures that discrete
187 weather patterns are smoothed out.

188 2.2 Inverse Lagrangian analysis

189 The wind fields from MarsWRF are used to drive the Stochastic Time-Inverted
190 Lagrangian Transport (STILT) Lagrangian Particle Dispersion Model (Lin et al., 2003;
191 Fasoli et al., 2018) to simulate plume transport and dispersion. STILT is based on the
192 Hybrid Single Particle Lagrangian Integrated Trajectory (HYSPLIT) model (Draxler and
193 Hess, 1998; Stein et al., 2015) that is extensively used in air quality, volcanic ash and
194 industrial plume modeling, and STILT inherits all of the validated components of its
195 predecessor. In its application, STILT transports an ensemble of computational particles
196 (ten thousand particles in each simulation in this study) from the site of the detector (here,
197 the location of the *Curiosity* rover) using time-reversed grid-scale wind plus a
198 parameterized subgrid-scale turbulent velocity (Hanna, 1984). The timestep in STILT is
199 determined dynamically based on the wind field, and typically ranges between one
200 minute and ten minutes. When combined with a GCM, STILT linearly interpolates the
201 simulated bulk wind from the GCM grid points to the precise positions of each particle at
202 each timestep, and then displaces the particles according to the reversed wind arrow.
203 Meanwhile, STILT adds a random velocity component, determined by a Markov chain
204 process based statistically on the simulated meteorological conditions, to the bulk wind
205 velocity. The random velocity represents turbulent motions that are unresolved by the
206 GCM and results in dispersion of the particle cloud (Fig. S3). Additionally, vertical
207 mixing in the PBL is parameterized by vertically redistributing particles to random
208 altitudes within the PBL (Fig. S4). In the hyper-near field around the detector, an

209 “effective mixing depth” smaller than the PBL thickness is calculated based on the
210 homogeneous turbulence theory (Fasoli et al., 2018). This will prevent the particles
211 released near the surface from ascending to the top of the PBL instantaneously.

212 At every timestep in a back-trajectory simulation (which corresponds to an
213 emission time), STILT tallies the instantaneous particle density in the PBL at all locations
214 and generates a “footprint” map in units of ppbv μmol^{-1} (Lin et al., 2003), which
215 quantifies the contribution of unit methane emission flux from an emission site to the
216 methane mole fraction at the detector. The STILT footprint is proportional to the column-
217 integrated particle number density within the PBL and the molar mass of air, and
218 inversely proportional to the PBL thickness and the average air density within the PBL
219 (Lin et al., 2003). The value of the footprint at an emission site is equal to the prospected
220 methane mole fraction in the unit of ppbv above the ~ 0.41 ppbv background level
221 induced by 1 μmol of methane emission at that emission site. High footprints indicate
222 regions where the emission casts strong influence over the detection, or in brief, the
223 upstream regions. Since the circulation pattern changes all the time, the footprint values
224 at the same emission site at different emission times are also different. If integrated over a
225 certain period of emission time, the footprints will measure the influence of a constant-
226 flux emission in that period of emission time on a detection, and the pattern of the time-
227 integrated footprints will show all upstream regions.

228 In computing the footprints, the domain is first gridded horizontally (a grid that is
229 separate from that of the GCM) so that STILT can count the number of particles within
230 each horizontal grid and calculate the particle density at all horizontal locations. The
231 resolution of this grid becomes the resolution of the footprints, and hence the resolution

232 of the emission regions. We use 2° as the resolution for the domain from 80°S to 80°N
233 and from 60°E eastward to 140°W . For the subdomain from 17.6°S to 8.4°N , from
234 124.2°E to 150.4°E , we use a higher resolution of 0.2° , or ~ 11.8 km. For the subdomain
235 from 6.64°S to 3.72°S , from 136.24°E to 139.16°E , we use a further higher resolution of
236 0.02° , or ~ 1.18 km. We note that the definition of the STILT footprint in this study is
237 slightly different from that in Lin et al. (2003). The new definition has excluded the
238 influence of the grid size and the timestep of the footprint calculation on the values of the
239 footprints.

240 STILT was originally designed for terrestrial use, and we adapted STILT so that it
241 can be used for Mars. The modifications include changes to planetary radius, gas
242 constant, angular rotation rate of the planet, surface gravity, dynamic viscosity of air,
243 mean free path of air, molecular weight of air, surface air pressure, specific heat capacity
244 of air, the map of land use, and the map of surface roughness length (Hébrard et al.,
245 2012), etc. We note that the Monin–Obukhov similarity theory for the PBL, along with
246 the adherence to the well-mixed criterion (Thomson, 1987), a manifestation of the second
247 law of thermodynamics, ensures that the physics and fluid dynamics underlying STILT
248 can be applied to all substantial planetary atmospheres, including the Martian
249 atmosphere.

250 **3 Results**

251 3.1 Categorization of methane spikes

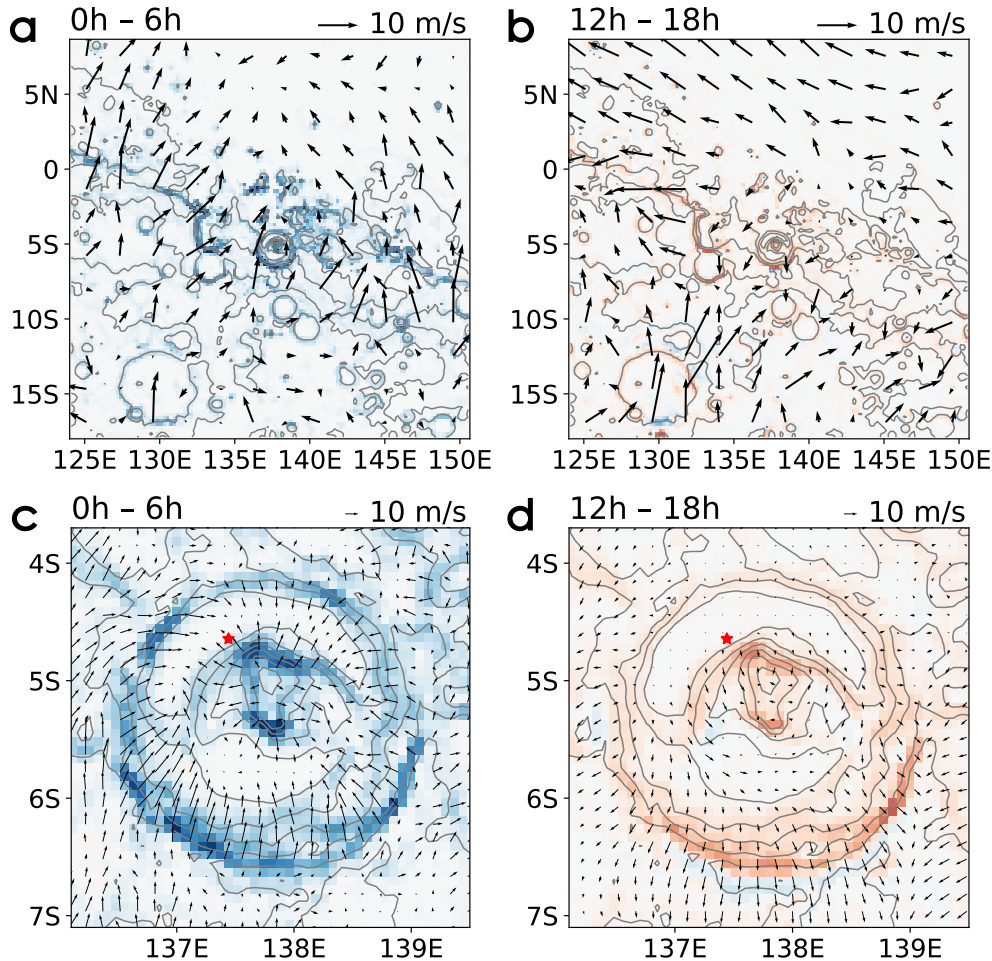
252 We focus on the six methane spikes reported by the TLS instrument (which is
253 referred to as the “detector” in the following text) during the 4.6 years of the *Curiosity*

254 mission through May 2017 (Fig. 1, Table S1). The six spikes can be categorized based on
255 the seasons and the time of day of their detections. In terms of seasons, Spikes 1 and 6
256 were detected from late northern fall into winter. Spikes 2–5 were detected in northern
257 spring. In terms of the time of day, Spikes 1 and 5 were detected in the early afternoon,
258 and Spikes 2, 3, 4 and 6 were detected between midnight and early morning. As a result,
259 Spikes 1 and 6 share similar seasonal, regional and global circulation patterns, as do
260 Spikes 2–5. Spikes 1 and 5 share similar diurnal crater circulation patterns, as do Spikes
261 2, 3, 4 and 6. The similarity in atmospheric circulation patterns also manifests itself in the
262 subsequent STILT footprint maps.

263 3.2 Atmospheric circulations

264 MarsWRF simulations show that the circulation at Gale crater consists of three
265 components – a global meridional overturning circulation, a regional circulation, and a
266 crater-scale circulation. Figure 2 shows an example of near-surface winds simulated by
267 MarsWRF. In northern winter, the rising branch of the global meridional overturning
268 circulation is centered in the southern hemisphere. Prevailing winds at the topographic
269 dichotomy next to Gale crater are southward and are particularly strong around 270° solar
270 longitude when Spike 6 was detected. In northern spring, the large-scale prevailing winds
271 at Gale crater are weak. The regional circulation is characterized by upslope northerlies
272 along the topographic dichotomy in the afternoon, and downslope southerlies in the
273 nighttime. The crater circulation is characterized by upslope winds along the inner crater
274 rim and the slope of Mount Sharp in the afternoon, and downslope winds in the
275 nighttime. The PBL thickness at Gale crater undergoes a daily cycle between a nighttime

276 minimum thickness of tens of meters, and a daytime maximum thickness of about three
 277 kilometers, similar to previous findings in Fonseca et al. (2018).



278

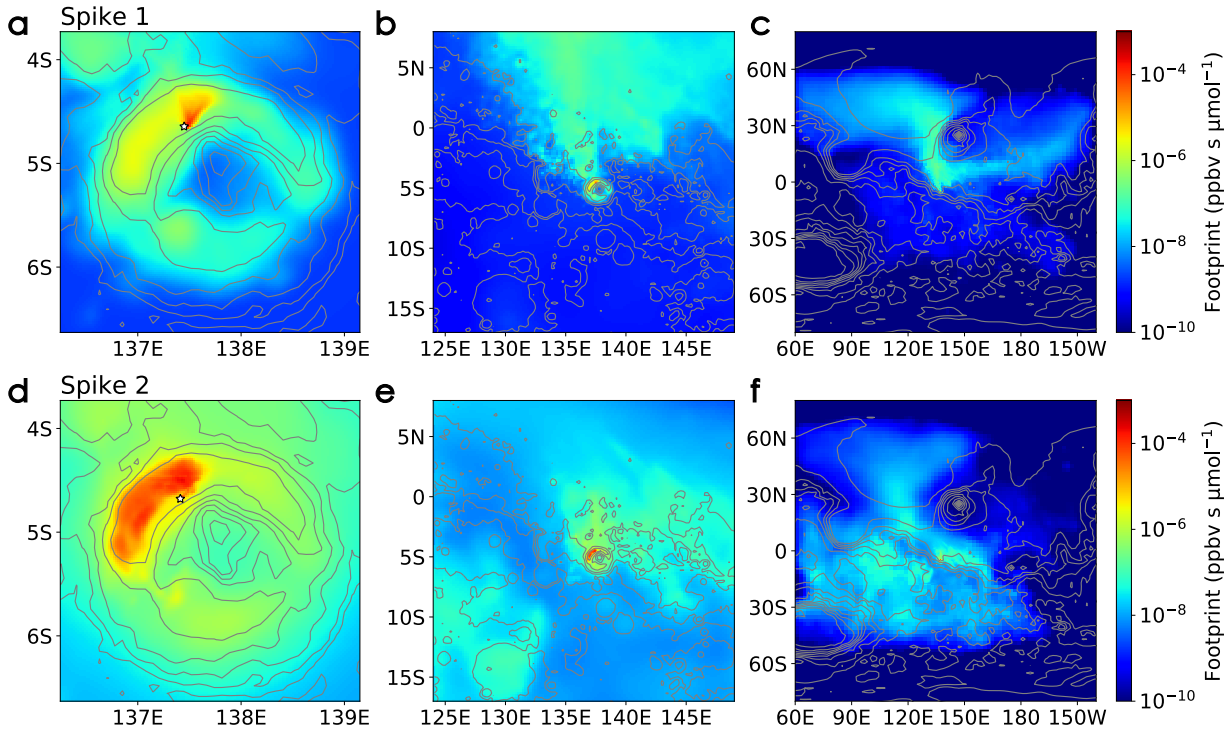
279 **Figure 2. Simulated winds in the bottom layer of MarsWRF at 81.84° solar longitude**
 280 **(concurrent with Spike 5).** The plotted data is an average over six hours as indicated by the
 281 time period on the upper left of each panel. (a) and (b) show the regional circulation, from which
 282 one can identify southwesterly downslope winds along the topographic dichotomy from
 283 midnight to sunrise, and northeasterly upslope winds from noon to sunset. (c) and (d) show the
 284 Gale crater circulation, from which one can identify downslope winds along the inner wall of the
 285 crater rim and along Mount Sharp from midnight to sunrise, and upslope winds from noon to

286 sunset. The crater circulation is well resolved by MarsWRF. Red colors show rising air. Blue
287 colors show sinking air. Contours show surface elevation. Red stars mark the position of
288 *Curiosity*.

289 3.3 Identifying upstream regions

290 Figure 3 shows the time-integrated footprints for Spikes 1 and 2. Refer to Fig. 5
291 and Fig. S5 for the footprints for Spikes 3–6. Within Gale crater, the strongest footprint
292 of Spike 1 lies to the north of the TLS detector (Fig. 3a), which is also the case for Spike
293 5 (Fig. S5g). This means that these two early-afternoon measurements are both more
294 sensitive to the emission from the north compared to the emission from other directions.
295 The similarity in the footprints for Spikes 1 and 5 is consistent with the similarity in the
296 early-afternoon crater-scale circulation patterns at the *Curiosity* site, in which northerlies
297 dominate, although Spikes 1 and 5 were detected in different seasons. For Spike 2, the
298 strongest footprint lies on the entire northwestern crater floor (Fig. 3d). This is also the
299 case for Spikes 3, 4, and 6 (Fig. 5d, Fig. S5a, d), although there are some finer spatial
300 patterns in the footprints for Spike 6. These four spikes were all detected in the nighttime
301 when the PBL was shallow. The released particles are confined within the PBL and
302 therefore imprint almost equally strong footprints onto the entire northwestern crater

303 floor as they are transported backwards in time. In other words, a nighttime detection is
 304 sensitive to the emission from any place on the northwestern crater floor.



305

306 **Figure 3. Influence of emission fluxes at any emission site on (a–c) Spike 1 and (d–f) Spike**
 307 **2, shown in (a, d) the crater scale, (b, e) the regional scale, and (c, f) the hemispherical**
 308 **scale. Colors show STILT footprints integrated backwards in time over thirty sols. High values**
 309 **of footprints indicate upstream regions. The values of the footprints are equal to the prospected**
 310 **TLS methane signals in ppbv above the ~ 0.41 ppbv background after a thirty-sol constant-flux**
 311 **methane emission event with an emission flux of $1 \mu\text{mol s}^{-1}$ occurs at one emission site. Stars in**
 312 **(a) and (d) mark the positions of *Curiosity*.**

313 Outside Gale crater, the strongest footprint for Spike 1 lies to the north of the
 314 crater, as a result of the prevailing regional-scale northerlies in this season (Fig. 3b). This
 315 is also true for Spike 6 (Fig. 5e). This shows that for these two spikes, if a methane

316 emission region exists in the neighborhood of Gale crater (but outside the crater), it is
317 most likely located to the north of the crater. The locations of the upstream regions for
318 Spike 2 are, however, less definitive. The strongest footprints for Spike 2 cover the
319 regions in the first and third quadrants of Gale crater (Fig. 3e). This is also the case for
320 Spikes 3–5 (Fig. S5b, e, h). Despite this ambiguity, the strongest footprints for all the six
321 spikes overlap in a region within 300 km to the north of Gale crater. It is noteworthy that
322 the “E8” and “ESE” regions, suggested as the most likely emission regions for Spike 1
323 (Giuranna et al., 2019), do not bear strong footprints in our study and are hence not
324 identified as the preferred upstream regions for Spike 1 (Fig. 3b).

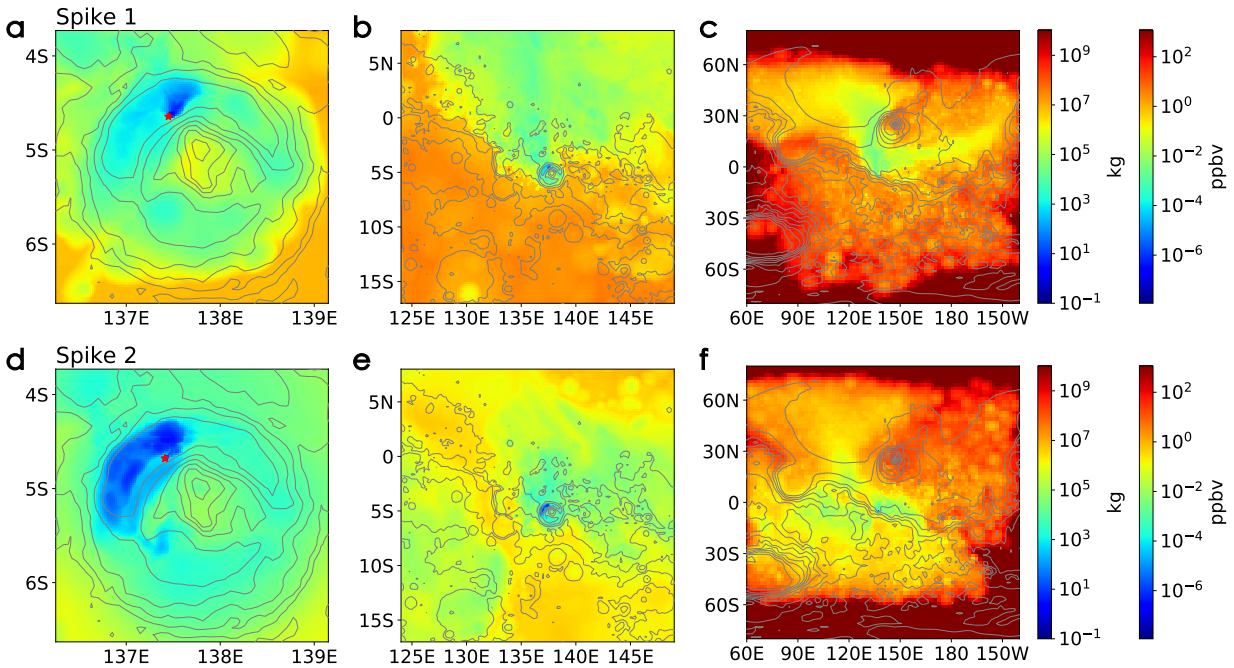
325 Further zooming out to the hemispherical scale, the strongest footprints for Spike
326 1 extend from Elysium Planitia towards two directions – one heading for the north along
327 the western side of Elysium Mons to Utopia Planitia, and the other heading for the east
328 along the southern side of Elysium Mons to Amazonis Planitia (Fig. 3c). This is also the
329 case for Spike 6, although the northern branch appears more prominent (Fig. 5f). This
330 suggests that the aforementioned large-scale geographic units are more likely to be the
331 emission regions than other large-scale geographic units for Spikes 1 and 6. For Spikes
332 2–5, the strong footprints cover many large-scale geographic units around Gale crater
333 (Fig. 3f, Fig. S5c, f, i), including the aforementioned Elysium Planitia and Utopia
334 Planitia.

335 3.4 Minimum methane emission

336 Based on the footprints, the minimum amount of methane emitted from any
337 emission site that could give rise to the observed methane spikes can be calculated. TLS’s

338 ~0.41 ppbv background level is first subtracted from the six methane spikes. The
339 remainder of the signals must then be a consequence of recent emission. It is unknown
340 whether the emission was continuous, intermittent, or episodic, but to put a lower bound
341 on the required methane emission, we can assume the emission was instantaneous and
342 occurred at the exact moment when an emission site had the strongest influence on a
343 detection. Then, dividing each methane signal (with the background signal subtracted) by
344 the maximum footprint at an emission site yields the minimum amount of methane
345 emitted from that emission site required by the methane signal (Fig. 4). Upstream
346 regions, which show up with the highest footprint values in Fig. 3, now bear the smallest
347 values in Fig. 4, the latter meaning that they can more easily produce a methane signal.
348 For example, the northwestern crater floor (the blue region in Fig. 4d) is able to produce
349 Spike 2 by emitting only about a hundred kilograms of methane, which will result in an
350 increase of $\sim 10^{-5}$ ppbv in the global mean methane concentration, assuming the emission
351 occurred at the exact moment when it cast the highest influence over the detection. In
352 contrast, if Spike 2 results from an emission event in Utopia Planitia, at least several
353 millions of kilograms of methane must have been emitted, which will result in an

354 increase of several hundreds of pptv (parts-per-trillion-by-volume, $1 \text{ pptv} = 10^{-3} \text{ ppbv}$) in
 355 the global mean methane concentration (Fig. 4f).



356

357 **Figure 4. The minimum amount of methane emitted from different locations that can**
 358 **produce (a–c) Spike 1 and (d–f) Spike 2.** The emission is assumed to occur at the moment
 359 when an emission site has the strongest influence on a detection. The left colorbars show the
 360 minimum mass of emitted methane as required by the magnitude of the spikes. The right
 361 colorbars show the increase in the globally averaged methane concentration after an
 362 aforementioned smallest emission event occurs. Stars in (a) and (d) mark the positions of
 363 *Curiosity*.

364 TGO's 0.02 ppbv upper limit (Montmessin et al., 2021), interpreted as the upper
 365 limit on the average methane concentration in the Martian atmosphere, if combined with
 366 the 330-year lifetime from standard photochemical models (Lefèvre and Forget, 2009),
 367 implies that on average no more than 6×10^{-5} ppbv of methane (or ~ 520 kg of methane) is

368 replenished every year. Then, during the 4.6 years of TLS operation, on average, no more
369 than $\sim 2.8 \times 10^{-4}$ ppbv (or ~ 2400 kilograms) was emitted into the atmosphere. Assuming
370 the six methane spikes result from six emission events, on average, each of them can emit
371 no more than ~ 400 kilograms of methane; otherwise, they would have resulted in a
372 significant and potentially observable rise in the background methane concentration.
373 Only the blue areas in Fig. 4 are such qualified areas that are able to produce a methane
374 spike with the observed mole fraction by emitting 400 kilograms of methane. More
375 quantitative analysis shows that the “qualified areas” are only 1300 km^2 in total, about
376 7% the total area of Gale crater (Fig. S10). This means that without fast removal
377 mechanisms that can significantly reduce the methane lifetime, the methane emission site
378 that is responsible for the TLS methane spikes has to be located within the 1300 km^2
379 around the *Curiosity* site inside Gale crater, and no other emission sites can exist over the
380 planet. This is the only way that the TLS spikes and the TGO non-detections can be
381 reconciled. The 1300 km^2 area is probably still an overestimate, as the assumed situation
382 where only six methane emission events occurred during the 4.6 years and all of them
383 were captured by the TLS measurements is almost impossible. The actual methane spike
384 frequency at the *Curiosity* site may be much higher, which will put a much lower upper
385 bound on the amount of methane emitted by a single emission event. In that case, the
386 qualified emission regions will be confined within even smaller areas that are very close
387 to the location of the *Curiosity* rover, such as the deep blue areas on the northwestern
388 crater floor in Fig. 4. Even the 1300 km^2 upper limit of the qualified emission region will
389 invoke an coincidence that *Curiosity* was sent to the vicinity of the only methane
390 emission hotspot on Mars. One possibility that does not invoke the coincidence is that

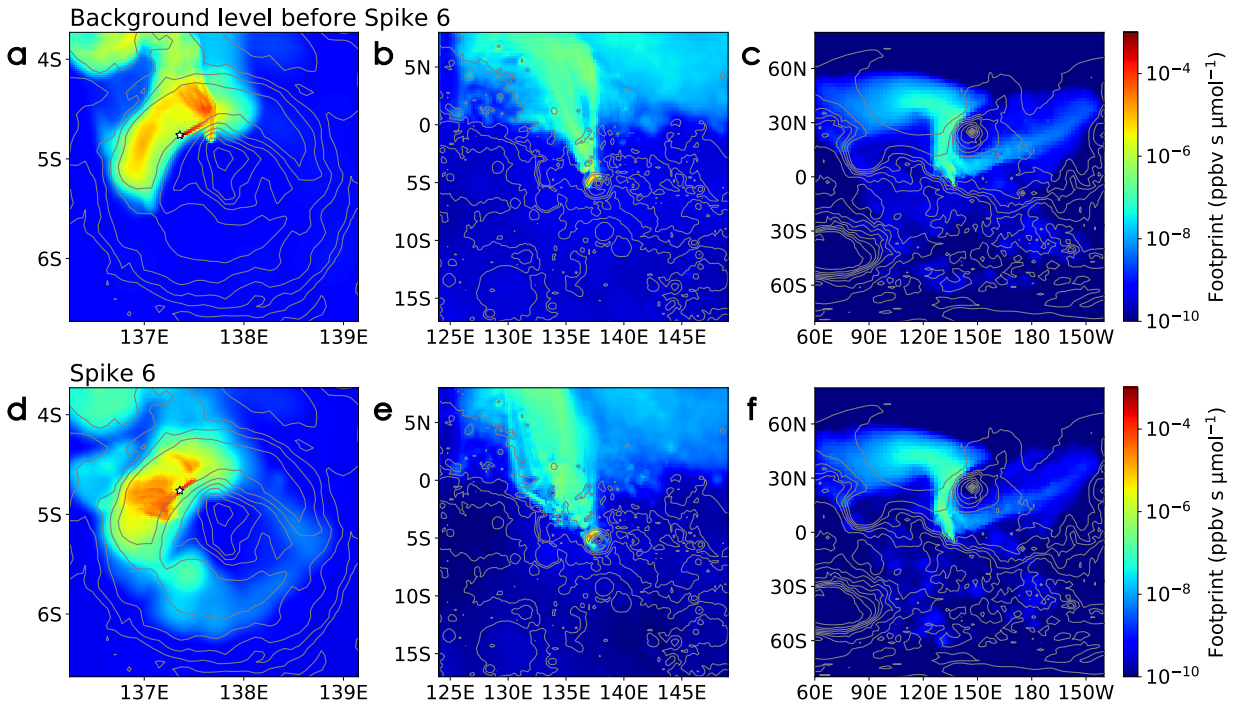
391 unknown, rapid methane removal mechanisms are at work. If the methane lifetime is
392 shorter than 330 years, more methane can be emitted into the atmosphere per year
393 without perturbing the long-term background methane concentration, and the emission
394 sites will have some freedom to be located at distant places outside Gale crater, most
395 likely in the upstream regions found in Section 3.3. Refer to Fig. S10 for a more
396 quantitative analysis on the required “coincidence” if we accept the results from both
397 TLS and TGO and the 330-year methane lifetime from classical models. To summarize,
398 under the three assumptions – 1. TLS’s methane spikes are real, 2. TGO’s upper limits
399 are real and they represent the upper limit of the methane abundance throughout the
400 Martian atmosphere, and 3. the methane lifetime is ~330 years – there will be only one
401 methane emission region over the entire globe, and it is within an area of 1300 km²
402 around the *Curiosity* site in northwestern Gale crater. This may just be a coincidence, as
403 Gale crater was carefully selected as the landing site for the *Curiosity* rover based on its
404 unique geological context (e.g., Grotzinger et al., 2015). Otherwise, at least one of the
405 three assumptions above needs to be reevaluated.

406 3.5 Consecutive methane measurements

407 More precise emission site identification is possible when we make use of
408 consecutive methane measurements that reported a large difference in methane
409 abundances. At ~266° solar longitude in Mars Year 33, two measurements were
410 consecutively performed within a few hours. The first measurement started at ~01:30
411 local time and detected a 0.332 ppbv signal, close to the background level. Only a few
412 hours later, the second measurement at ~06:30 local time detected Spike 6 with 5.55
413 ppbv. One possible explanation for the rapid increase in the ambient methane

414 concentration is the initiation of an emission event between the two measurements. Here,
415 we focus on another possibility that a change in wind directions between the two
416 measurements induced the temporal variability of the methane signals. If an emission
417 event occurred before the two methane measurements, it would produce a methane signal
418 only if the emission site was located in the upstream region of the detector at the time of
419 emission. Figure 5 shows a comparison between the time-integrated footprints for Spike
420 6 and those for the background level. A significant difference can be found between the
421 upstream regions within Gale crater (Fig. 5a, d). On the northwestern crater floor, the
422 upstream region of Spike 6, indicated by high footprint values, primarily lies to the west
423 and the southwest of *Curiosity* rover, whereas the upstream region of the background
424 level primarily lies to the northeast of the rover. Therefore, the region to the west and the
425 southwest of *Curiosity* in northwestern Gale crater is identified as a highly probable

426 location of an emission site. There are not significant differences between the upstream
 427 regions at larger scales (Fig. 5b, e, and Fig. 5c, f).



428

429 **Figure 5. Comparison of the footprints for the background level and for Spike 6, both**
 430 **measured at $\sim 266^\circ$ solar longitude in Mars Year 33.** Panels (a–c) show the STILT footprint
 431 for the background concentration. (d–f) show the STILT footprint for Spike 6. The stars in (a)
 432 and (d) show the positions of *Curiosity*. An emission site with weak influence on the background
 433 level and strong influence on Spike 6 will be bearing a small footprint for the former and a large
 434 footprint for the latter. Comparing (a) and (d), regions to the west and the southwest of *Curiosity*
 435 on the northwestern crater floor are such regions. The differences between (b) and (e) and
 436 between (c) and (f) at the larger scales are not significant.

437 We note that this method based on consecutive methane measurements is able to
 438 precisely constrain the location of a nearby emission site, but it requires consecutive

439 measurements performed within a short period of time, shorter than a few days and
440 optimally a few hours. Fortunately, the measurement strategy of TLS, which often
441 performs paired measurements within a few hours, meets this requirement.

442 **4 Conclusions**

443 In conclusion, if we trust the methane abundances detected by both TLS and TGO and
444 accept the 330-year methane lifetime from known photochemistry, our back-trajectory modeling
445 for atmospheric transport strongly supports surface emission sites in the vicinity of the *Curiosity*
446 rover in northwestern Gale crater. This may invoke a coincidence that we selected a landing site
447 for *Curiosity* that is located next to an active methane emission site. Other possibilities that does
448 not invoke the coincidence include the existence of fast methane removal mechanisms that are
449 unknown to date, and false positives of TLS and false negatives of TGO. Should future studies
450 confirm the existence of heterogeneous pathways or other unknown photochemical processes for
451 methane destruction, the methane emission sites can be located outside Gale crater, and most
452 likely to the north of the crater. Continuing the TLS and the TGO measurements of methane
453 concentration at Gale crater still seems to be the best move for now.

454 Our study demonstrates the feasibility and the advantages of applying the inverse
455 Lagrangian modeling technique to source localization problems on other planets. Methane
456 abundance data from future in situ measurements, especially those collected in consecutive
457 measurements performed within a few hours, would further improve the source localization.

458 **Acknowledgments, Samples, and Data**

459 A portion of this research was carried out at the Jet Propulsion Laboratory, California Institute of
460 Technology, under contract with NASA. Government sponsorship acknowledged. Y. L. Y

461 acknowledges the President's and Director's Research and Development Fund and the support
462 from the Virtual Planetary Laboratory at the University of Washington that is funded via NASA
463 Astrobiology Program Grant No. 80NSSC18K0829. Resources supporting this work were
464 provided by the NASA High-End Computing (HEC) Program through the NASA Advanced
465 Supercomputing (NAS) Division at Ames Research Center.

466 A file that lists all the relevant conditions and parameters used in the MarsWRF simulations can
467 be found at the CaltechDATA repository via <https://doi.org/10.22002/D1.2026>. The original
468 STILT model is available at its website <https://uataq.github.io/stilt/#/>. A list of modifications to
469 the original STILT model based on the conditions of Mars can be found at the CaltechDATA
470 repository via <https://doi.org/10.22002/D1.2026>. The STILT footprint files used to generate
471 Figure 3–5 in this study are available at the CaltechDATA repository via
472 <https://doi.org/10.22002/D1.2025>.

473 **References**

- 474 1. Aoki, S., Richter, M. J., DeWitt, C., Boogert, A., Encrenaz, T., Sagawa, H., et al. (2018).
475 Stringent upper limit of CH₄ on Mars based on SOFIA/EXES observations. *Astronomy &*
476 *Astrophysics*, *610*, A78. <https://doi.org/10.1051/0004-6361/201730903>
- 477 2. Christensen, P. R., Bandfield, J. L., Hamilton, V. E., Ruff, S. W., Kieffer, H. H., Titus, T. N.,
478 et al. (2001). Mars Global Surveyor Thermal Emission Spectrometer experiment:
479 investigation description and surface science results. *Journal of Geophysical Research:*
480 *Planets*, *106*(E10), 23823-23871. <https://doi.org/10.1029/2000JE001370>
- 481 3. Cicerone, R. J., & Oremland, R. S. (1988). Biogeochemical aspects of atmospheric methane.
482 *Global Biogeochemical Cycles*, *2*(4), 299-327. <https://doi.org/10.1029/GB002i004p00299>
- 483 4. Draxler, R. R., & Hess, G. D. (1998). An overview of the HYSPLIT_4 modelling system for

- 484 trajectories. *Australian Meteorological Magazine*, 47(4), 295-308.
- 485 5. Fasoli, B., Lin, J. C., Bowling, D. R., Mitchell, L., & Mendoza, D. (2018). Simulating
486 atmospheric tracer concentrations for spatially distributed receptors: updates to the Stochastic
487 Time-Inverted Lagrangian Transport model's R interface (STILT-R version 2). *Geoscientific
488 Model Development*, 11(7), 2813-2824. <https://doi.org/10.5194/gmd-11-2813-2018>
- 489 6. Fonseca, R. M., Zorzano-Mier, M. P., & Martín-Torres, J. (2018). Planetary boundary layer
490 and circulation dynamics at Gale Crater, Mars. *Icarus*, 302, 537-559.
491 <https://doi.org/10.1016/j.icarus.2017.11.036>
- 492 7. Fonti, S., & Marzo, G. A. (2010). Mapping the methane on Mars. *Astronomy & Astrophysics*,
493 512, A51. <https://doi.org/10.1051/0004-6361/200913178>
- 494 8. Formisano, V., Atreya, S., Encrenaz, T., Ignatiev, N., & Giuranna, M. (2004). Detection of
495 methane in the atmosphere of Mars. *Science*, 306(5702), 1758-1761.
496 <https://doi.org/10.1126/science.1101732>
- 497 9. Geminale, A., Formisano, V., & Giuranna, M. (2008). Methane in Martian atmosphere:
498 average spatial, diurnal, and seasonal behaviour. *Planetary and Space Science*, 56(9), 1194-
499 1203. <https://doi.org/10.1016/j.pss.2008.03.004>
- 500 10. Gerbig, C., Lin, J. C., Wofsy, S. C., Daube, B. C., Andrews, A. E., Stephens, B. B., et al.
501 (2003). Toward constraining regional-scale fluxes of CO₂ with atmospheric observations
502 over a continent: 2. Analysis of COBRA data using a receptor-oriented framework. *Journal
503 of Geophysical Research: Atmospheres*, 108(D24). <https://doi.org/10.1029/2003JD003770>
- 504 11. Giuranna, M., Viscardy, S., Daerden, F., Neary, L., Etiope, G., Oehler, D., et al. (2019).
505 Independent confirmation of a methane spike on Mars and a source region east of Gale
506 Crater. *Nature Geoscience*, 12(5), 326-332. <https://doi.org/10.1038/s41561-019-0331-9>

- 507 12. Gough, R. V., Tolbert, M. A., McKay, C. P., & Toon, O. B. (2010). Methane adsorption on a
508 Martian soil analog: An abiogenic explanation for methane variability in the Martian
509 atmosphere. *Icarus*, 207(1), 165-174. <https://doi.org/10.1016/j.icarus.2009.11.030>
- 510 13. Grotzinger, J. P., Gupta, S., Malin, M. C., Rubin, D. M., Schieber, J., Siebach, K., et al.
511 (2015). Deposition, exhumation, and paleoclimate of an ancient lake deposit, Gale crater,
512 Mars. *Science*, 350(6257). <https://doi.org/10.1126/science.aac7575>
- 513 14. Guzewich, S. D., Talaat, E. R., Toigo, A. D., Waugh, D. W., & McConnochie, T. H. (2013).
514 High-altitude dust layers on Mars: Observations with the Thermal Emission
515 Spectrometer. *Journal of Geophysical Research: Planets*, 118(6), 1177-1194.
516 <https://doi.org/10.1002/jgre.20076>
- 517 15. Guzewich, S. D., Wilson, R. J., McConnochie, T. H., Toigo, A. D., Banfield, D. J., & Smith,
518 M. D. (2014). Thermal tides during the 2001 Martian global-scale dust storm. *Journal of*
519 *Geophysical Research: Planets*, 119(3), 506-519. <https://doi.org/10.1002/2013JE004502>
- 520 16. Hanna, S. R. (1984). Applications in air pollution modeling. In *Atmospheric turbulence and*
521 *air pollution modelling* (pp. 275-310). Springer, Dordrecht. [https://doi.org/10.1007/978-94-](https://doi.org/10.1007/978-94-010-9112-1_7)
522 [010-9112-1_7](https://doi.org/10.1007/978-94-010-9112-1_7)
- 523 17. Hébrard, E., Listowski, C., Coll, P., Marticorena, B., Bergametti, G., Määttänen, A., et al.
524 (2012). An aerodynamic roughness length map derived from extended Martian rock
525 abundance data. *Journal of Geophysical Research: Planets*, 117(E4).
526 <https://doi.org/10.1029/2011JE003942>
- 527 18. Hu, R., Bloom, A. A., Gao, P., Miller, C. E., & Yung, Y. L. (2016). Hypotheses for near-
528 surface exchange of methane on Mars. *Astrobiology*, 16(7), 539-550.
529 <https://doi.org/10.1089/ast.2015.1410>

- 530 19. Kite, E. S., Gao, P., Goldblatt, C., Mischna, M. A., Mayer, D. P., & Yung, Y. L. (2017).
531 Methane bursts as a trigger for intermittent lake-forming climates on post-Noachian
532 Mars. *Nature Geoscience*, *10*(10), 737-740. <https://doi.org/10.1038/ngeo3033>
- 533 20. Knak Jensen, S. J., Skibsted, J., Jakobsen, H. J., Inge, L., Gunnlaugsson, H. P., Merrison, J.
534 P., et al. (2014). A sink for methane on Mars? The answer is blowing in the
535 wind. *Icarus*, *236*, 24-27. <https://doi.org/10.1016/j.icarus.2014.03.036>
- 536 21. Knutsen, E. W., Villanueva, G. L., Liuzzi, G., Crismani, M. M., Mumma, M. J., Smith, M.
537 D., et al. (2021). Comprehensive investigation of Mars methane and organics with
538 ExoMars/NOMAD. *Icarus*, *357*, 114266. <https://doi.org/10.1016/j.icarus.2020.114266>
- 539 22. Korablev, O., Vandaele, A. C., Montmessin, F., Fedorova, A. A., Trokhimovskiy, A., Forget,
540 F., et al. (2019). No detection of methane on Mars from early ExoMars Trace Gas Orbiter
541 observations. *Nature*, *568*(7753), 517-520. <https://doi.org/10.1038/s41586-019-1096-4>
- 542 23. Kort, E. A., Eluszkiewicz, J., Stephens, B. B., Miller, J. B., Gerbig, C., Nehrkorn, T., et al.
543 (2008). Emissions of CH₄ and N₂O over the United States and Canada based on a receptor-
544 oriented modeling framework and COBRA-NA atmospheric observations. *Geophysical*
545 *Research Letters*, *35*(18). <https://doi.org/10.1029/2008GL034031>
- 546 24. Krasnopolsky, V. A. (2012). Search for methane and upper limits to ethane and SO₂ on
547 Mars. *Icarus*, *217*(1), 144-152. <https://doi.org/10.1016/j.icarus.2011.10.019>
- 548 25. Krasnopolsky, V. A., Maillard, J. P., & Owen, T. C. (2004). Detection of methane in the
549 martian atmosphere: evidence for life?. *Icarus*, *172*(2), 537-547.
550 <https://doi.org/10.1016/j.icarus.2004.07.004>
- 551 26. Lee, C., Lawson, W. G., Richardson, M. I., Anderson, J. L., Collins, N., Hoar, T., &
552 Mischna, M. (2011). Demonstration of ensemble data assimilation for Mars using DART,

- 553 MarsWRF, and radiance observations from MGS TES. *Journal of Geophysical Research:*
554 *Planets*, 116(E11). <https://doi.org/10.1029/2011JE003815>
- 555 27. Lefèvre, F., & Forget, F. (2009). Observed variations of methane on Mars unexplained by
556 known atmospheric chemistry and physics. *Nature*, 460(7256), 720-723.
557 <https://doi.org/10.1038/nature08228>
- 558 28. Lin, J. C., Gerbig, C., Wofsy, S. C., Andrews, A. E., Daube, B. C., Davis, K. J., & Grainger,
559 C. A. (2003). A near-field tool for simulating the upstream influence of atmospheric
560 observations: The Stochastic Time-Inverted Lagrangian Transport (STILT) model. *Journal of*
561 *Geophysical Research: Atmospheres*, 108(D16). <https://doi.org/10.1029/2002JD003161>
- 562 29. Lin, J. C., Gerbig, C., Wofsy, S. C., Andrews, A. E., Daube, B. C., Grainger, C. A., et al.
563 (2004). Measuring fluxes of trace gases at regional scales by Lagrangian observations:
564 Application to the CO₂ Budget and Rectification Airborne (COBRA) study. *Journal of*
565 *Geophysical Research: Atmospheres*, 109(D15). <https://doi.org/10.1029/2004JD004754>
- 566 30. Lin, J. C., Brunner, D., Gerbig, C., Stohl, A., Luhar, A. K., & Webley, P. W. (2012).
567 Lagrangian Modeling of the Atmosphere. *Geophys. Monogr.*, 200, 349.
568 <https://doi.org/10.1029/GM200>
- 569 31. Macatangay, R., Warneke, T., Gerbig, C., Körner, S., Ahmadov, R., Heimann, M., &
570 Notholt, J. (2008). A framework for comparing remotely sensed and in-situ CO₂
571 concentrations. *Atmospheric Chemistry and Physics*, 8(9), 2555-2568.
572 <https://doi.org/10.5194/acp-8-2555-2008>
- 573 32. Mahaffy, P. R., Webster, C. R., Cabane, M., Conrad, P. G., Coll, P., Atreya, S. K., et al.
574 (2012). The sample analysis at Mars investigation and instrument suite. *Space Science*
575 *Reviews*, 170(1), 401-478. <https://doi.org/10.1007/s11214-012-9879-z>

- 576 33. Mallia, D. V., Lin, J. C., Urbanski, S., Ehleringer, J., & Nehrkorn, T. (2015). Impacts of
577 upwind wildfire emissions on CO, CO₂, and PM_{2.5} concentrations in Salt Lake City,
578 Utah. *Journal of Geophysical Research: Atmospheres*, 120(1), 147-166.
579 <https://doi.org/10.1002/2014JD022472>
- 580 34. Mischna, M. A., Allen, M., Richardson, M. I., Newman, C. E., & Toigo, A. D. (2011).
581 Atmospheric modeling of Mars methane surface releases. *Planetary and Space*
582 *Science*, 59(2-3), 227-237. <https://doi.org/10.1016/j.pss.2010.07.005>
- 583 35. Montmessin, F., Korablev, O. I., Trokhimovskiy, A., Lefèvre, F., Fedorova, A. A., Baggio,
584 L., et al. (2021). A stringent upper limit of 20 pptv for methane on Mars and constraints on
585 its dispersion outside Gale crater. *Astronomy and Astrophysics-A&A*, published online.
586 <https://doi.org/10.1051/0004-6361/202140389>
- 587 36. Moores, J. E., Gough, R. V., Martinez, G. M., Meslin, P. Y., Smith, C. L., Atreya, S. K., et
588 al. (2019a). Methane seasonal cycle at Gale Crater on Mars consistent with regolith
589 adsorption and diffusion. *Nature Geoscience*, 12(5), 321-325.
590 <https://doi.org/10.1038/s41561-019-0313-y>
- 591 37. Moores, J. E., King, P. L., Smith, C. L., Martinez, G. M., Newman, C. E., Guzewich, S. D.,
592 et al. (2019b). The methane diurnal variation and microseepage flux at Gale crater, Mars as
593 constrained by the ExoMars Trace Gas Orbiter and Curiosity observations. *Geophysical*
594 *Research Letters*, 46(16), 9430-9438. <https://doi.org/10.1029/2019GL083800>
- 595 38. Mumma, M. J., Villanueva, G. L., Novak, R. E., Hewagama, T., Bonev, B. P., DiSanti, M.
596 A., et al. (2009). Strong release of methane on Mars in northern summer 2003. *Science*,
597 323(5917), 1041-1045. <https://doi.org/10.1126/science.1165243>

- 598 39. Newman, C. E., Gómez-Elvira, J., Marin, M., Navarro, S., Torres, J., Richardson, M. I., et al.
599 (2017). Winds measured by the Rover Environmental Monitoring Station (REMS) during the
600 Mars Science Laboratory (MSL) rover's Bagnold Dunes Campaign and comparison with
601 numerical modeling using MarsWRF. *Icarus*, 291, 203-231.
602 <https://doi.org/10.1016/j.icarus.2016.12.016>
- 603 40. Newman, C. E., Baker, M. M., Banfield, D. J., Banks, M., Karatekin, O., Navarro, S., et al.
604 (2020). *Using InSight Wind Data to Validate Atmospheric Models and Improve Predictions*
605 *for Other Locations on Mars*. Paper presented at the AGU Fall Meeting 2020, online.
- 606 41. Oehler, D. Z., & Etiope, G. (2017). Methane seepage on Mars: where to look and why.
607 *Astrobiology*, 17(12), 1233-1264. <https://doi.org/10.1089/ast.2017.1657>
- 608 42. Oze, C., & Sharma, M. (2005). Have olivine, will gas: serpentinization and the abiogenic
609 production of methane on Mars. *Geophysical Research Letters*, 32(10).
610 <https://doi.org/10.1029/2005GL022691>
- 611 43. Pla-García, J., Rafkin, S. C., Karatekin, Ö., & Gloesener, E. (2019). Comparing MSL
612 Curiosity rover TLS-SAM methane measurements with Mars Regional Atmospheric
613 Modeling System atmospheric transport experiments. *Journal of Geophysical Research:*
614 *Planets*, 124(8), 2141-2167. <https://doi.org/10.1029/2018JE005824>
- 615 44. Putzig, N. E., Mellon, M. T., Kretke, K. A., & Arvidson, R. E. (2005). Global thermal inertia
616 and surface properties of Mars from the MGS mapping mission. *Icarus*, 173(2), 325-341.
617 <https://doi.org/10.1016/j.icarus.2004.08.017>
- 618 45. Richardson, M. I., Toigo, A. D., & Newman, C. E. (2007). PlanetWRF: A general purpose,
619 local to global numerical model for planetary atmospheric and climate dynamics. *Journal of*
620 *Geophysical Research: Planets*, 112(E9). <https://doi.org/10.1029/2006JE002825>

- 621 46. Stein, A. F., Draxler, R. R., Rolph, G. D., & Stunder, B. J. (2015). B., Cohen, MD, and Ngan,
622 F.: NOAA'S HYSPLIT atmospheric transport and dispersion modeling system, *Bulletin of*
623 *the American Meteorological Society*, 96, 2059-2077. [https://doi.org/10.1175/BAMS-D-14-](https://doi.org/10.1175/BAMS-D-14-00110.1)
624 00110.1
- 625 47. Thomson, D. J. (1987). Criteria for the selection of stochastic models of particle trajectories
626 in turbulent flows. *Journal of fluid mechanics*, 180, 529-556.
627 <https://doi.org/10.1017/S0022112087001940>
- 628 48. Toigo, A. D., Lee, C., Newman, C. E., & Richardson, M. I. (2012). The impact of resolution
629 on the dynamics of the martian global atmosphere: Varying resolution studies with the
630 MarsWRF GCM. *Icarus*, 221(1), 276-288. <https://doi.org/10.1016/j.icarus.2012.07.020>
- 631 49. Webster, C. R., Mahaffy, P. R., Atreya, S. K., Flesch, G. J., Mischna, M. A., Meslin, P. Y., et
632 al. (2015). Mars methane detection and variability at Gale crater. *Science*, 347(6220), 415-
633 417. <https://doi.org/10.1126/science.1261713>
- 634 50. Webster, C. R., Mahaffy, P. R., Atreya, S. K., Moores, J. E., Flesch, G. J., Malespin, C., et al.
635 (2018). Background levels of methane in Mars' atmosphere show strong seasonal
636 variations. *Science*, 360(6393), 1093-1096. <https://doi.org/10.1126/science.aaq0131>
- 637 51. Webster, C. R., Mahaffy, P. R., Pla-Garcia, J., Rafkin, S. C., Moores, J. E., Atreya, S. K., et
638 al. (2021). Day-night differences in Mars methane suggest nighttime containment at Gale
639 crater. *Astronomy and Astrophysics*, 650 (2021) A166. [https://doi.org/10.1051/0004-](https://doi.org/10.1051/0004-6361/202040030)
640 6361/202040030
- 641 52. Yung, Y. L., Chen, P., Nealon, K., Atreya, S., Beckett, P., Blank, J. G., et al. (2018).
642 Methane on Mars and habitability: challenges and responses. *Astrobiology*, 18(10), 1221-
643 1242. <https://doi.org/10.1089/ast.2018.1917>

Supporting Information for

**Mars Methane Sources in Northwestern Gale Crater Inferred from
Back-Trajectory Modeling**

5 **Table S1. TLS methane signals investigated in this study.** Adapted from Table S2 in Webster et al. (2018).

Name	Solar longitude (degrees)	Local time at Gale crater	<i>In situ</i> methane abundance (ppbv)
Spike 1	336.12	13:55	5.78
Spike 2	55.59	03:22	5.48
Spike 3	59.20	03:22	6.88
Spike 4	72.66	02:53	6.91
Spike 5	81.84	13:26	9.34
Background level before Spike 6	265.78	01:26	0.332
Spike 6	265.91	06:29	5.55

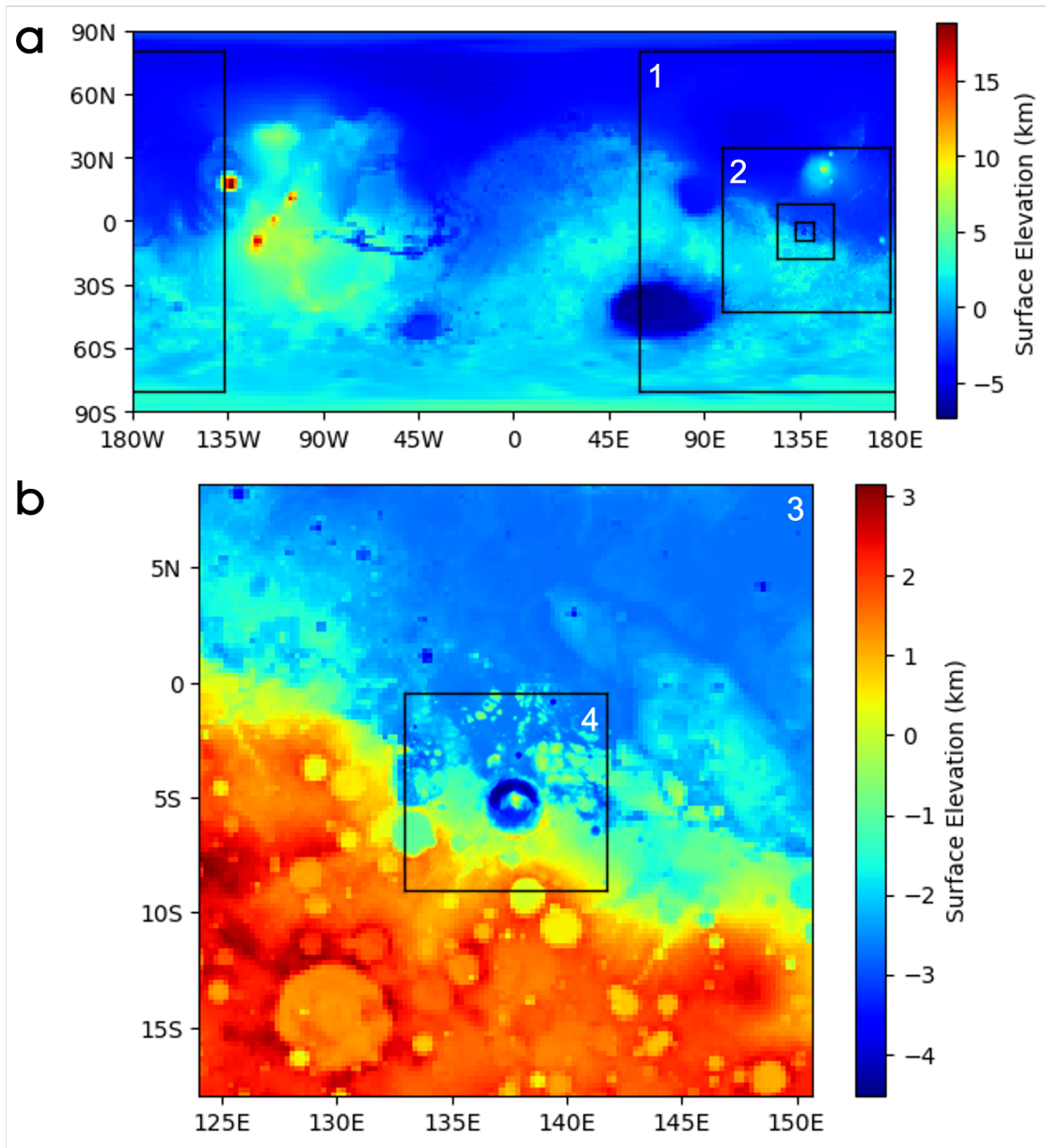


Fig. S1. MarsWRF domains on the four nesting levels. (a) Level 1, with a horizontal resolution of $2^\circ \times 2^\circ$ or $118 \text{ km} \times 118 \text{ km}$, and level 2, $0.67^\circ \times 0.67^\circ$ or $39 \text{ km} \times 39 \text{ km}$. **(b)** Level 3, $0.222^\circ \times 0.222^\circ$ or $13.1 \text{ km} \times 13.1 \text{ km}$, and level 4, $0.074^\circ \times 0.074^\circ$ or $4.4 \text{ km} \times 4.4 \text{ km}$. Colors show surface elevation in the corresponding horizontal resolutions of the four resolution levels.

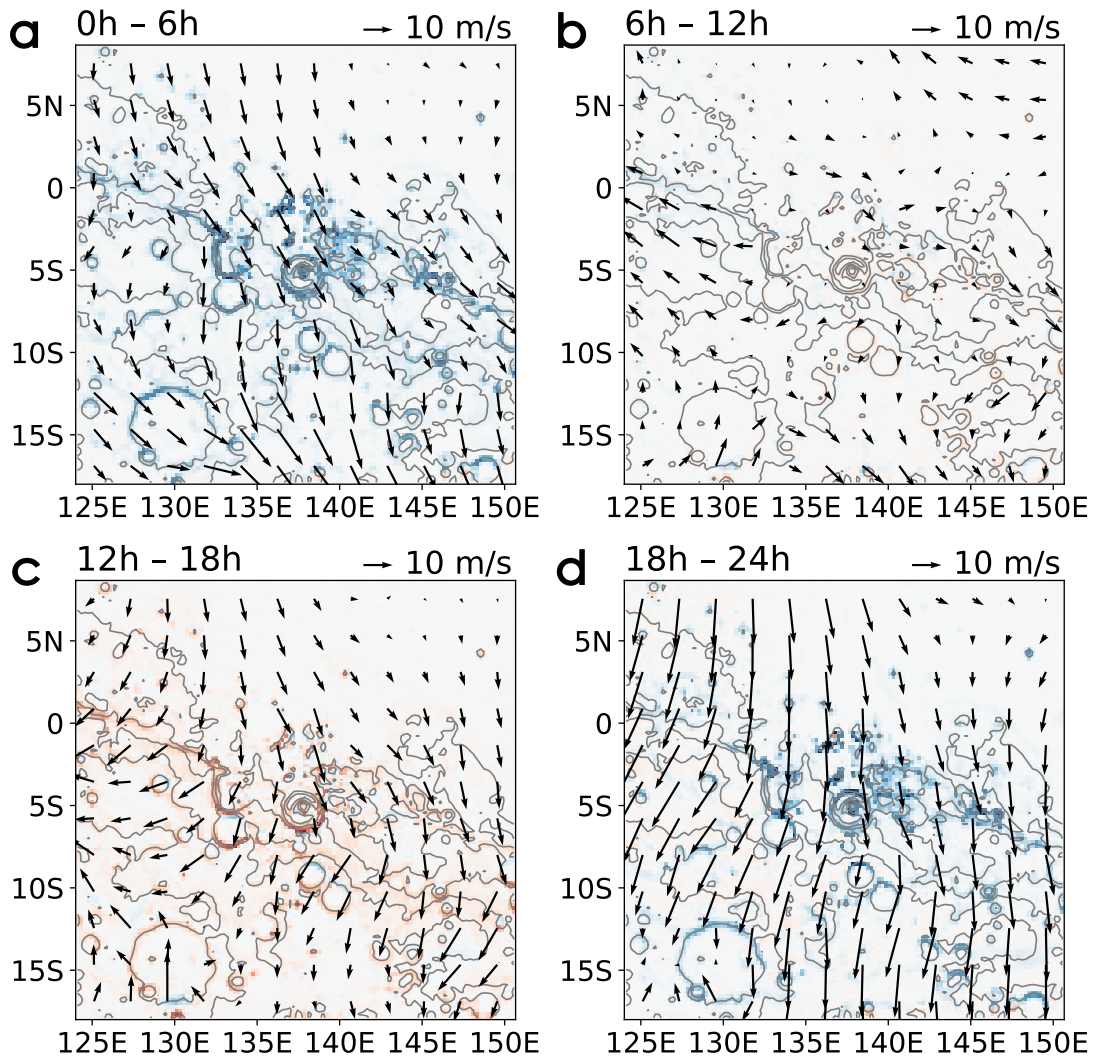


Fig. S2. MarsWRF-simulated winds averaged over the lowest 5 km of the atmosphere at 336.12° solar longitude (Spike 1). The plotted data is an average over six hours as indicated by the time period on the upper left of each subplot, and also an average over an ensemble of thirty-five sols. Weighted average by air density is performed in the vertical direction. Each arrow shows the horizontal wind averaged over a 131 km×131 km square. Red colors show rising air. Blue colors show sinking air. Contours show surface elevation. This figure can be directly compared to Fig. S17 in Giuranna et al. (2019). Between 00:00 and 06:00 local time and between 12:00 and 24:00 local time, the MarsWRF winds and the GEM-Mars winds are similar in directions – both of them are primarily northerlies, although the MarsWRF winds are stronger.

Between 06:00 and 12:00 local time, the GEM-Mars winds are weak easterlies, which was found responsible for transporting methane plumes from the regions to the east and the southeast of Gale crater to Gale (Giuranna et al., 2019). The MarsWRF winds in this time period are different, which are weak in general and do not show a dominant wind direction.

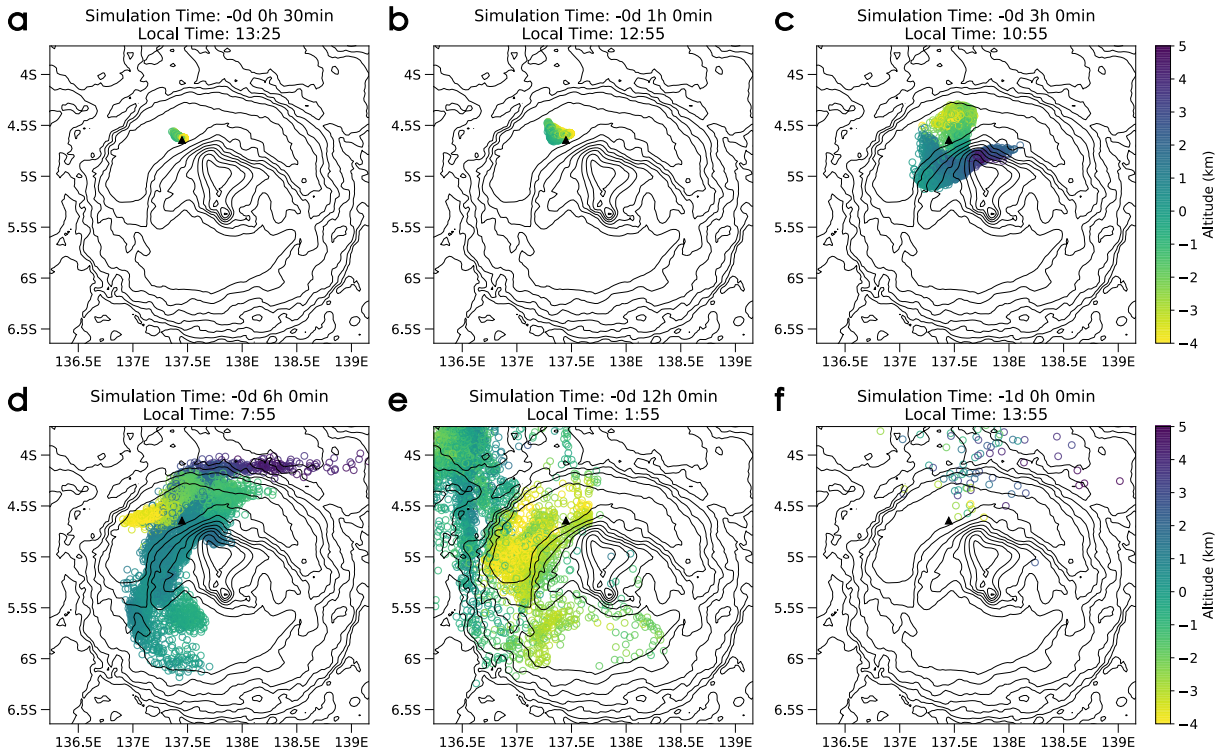


Fig. S3. Dispersion of backward-traveling particles within Gale crater (a) thirty minutes, (b) one hour, (c) three hours, (d) six hours, (e) twelve hours, and (f) one sol after particles are released. The STILT simulation is for Spike 1. Each circle shows the position of a single particle. Ten thousand particles are released in the simulation. Colors show the altitude of the particles relative to the Mars datum elevation. Contours show surface elevation. The black triangles mark the position of *Curiosity*. Almost all particles are ventilated out of Gale crater after one sol, indicating an exchange timescale of shorter than one sol, consistent with the findings in (Pla-García et al., 2019).

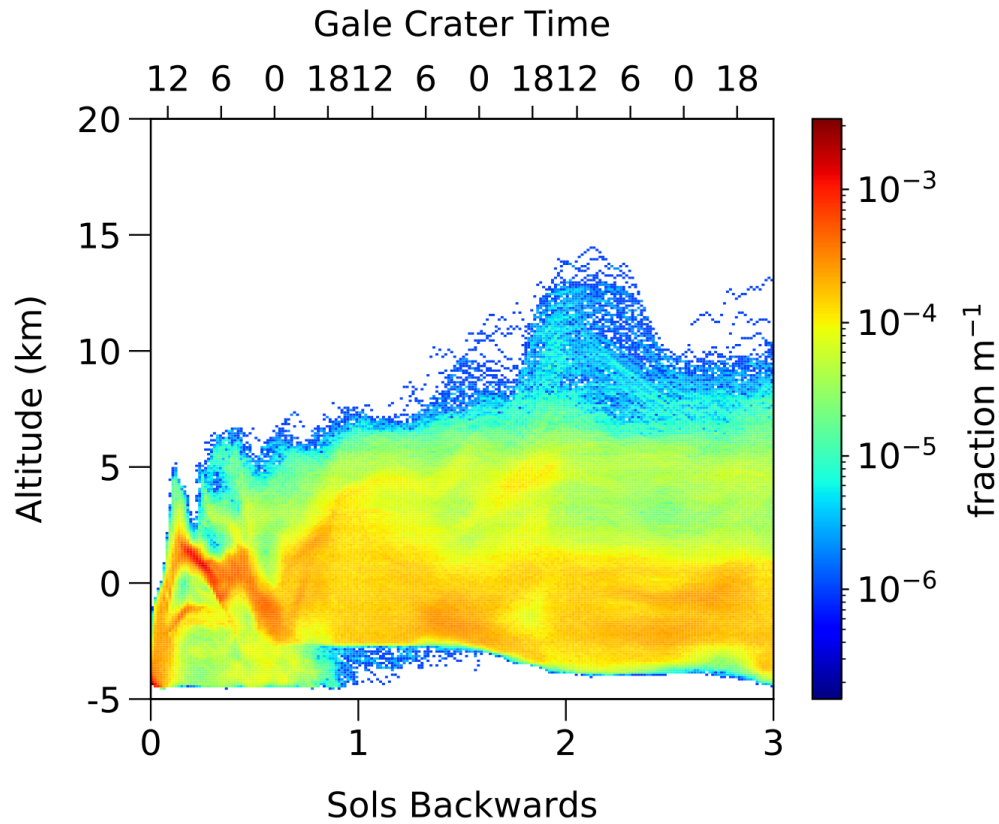


Fig. S4. Vertical dispersion of particles in a STILT simulation. An example simulation for Spike 1 is shown. Ten thousand particles are released in the simulation from the lower left corner of the figure. Colors show the fraction of the ten thousand particles with one-meter resolution in the vertical direction, indicating the number density of particles at different altitudes. Note that the particles are also dispersed in the horizontal direction, and almost all of the particles have left Gale crater one sol after the release (refer to Fig. S3). Immediately after the particle release, the majority of the particles climb up the northwestern slope of Mount Sharp, as is shown by the rapid ascent in this figure. This is consistent with the downslope wind along Mount Sharp in the early morning. In the daytime convective PBL, the convection parameterized in STILT randomly redistributes particles in the vertical direction. This results in a nearly homogeneous distribution of particles within the daytime PBL. Three sols after the release, some particles are still in

contact with the surface. Extending the simulation out to thirty sols ultimately produces a homogeneous distribution across the lower atmosphere.

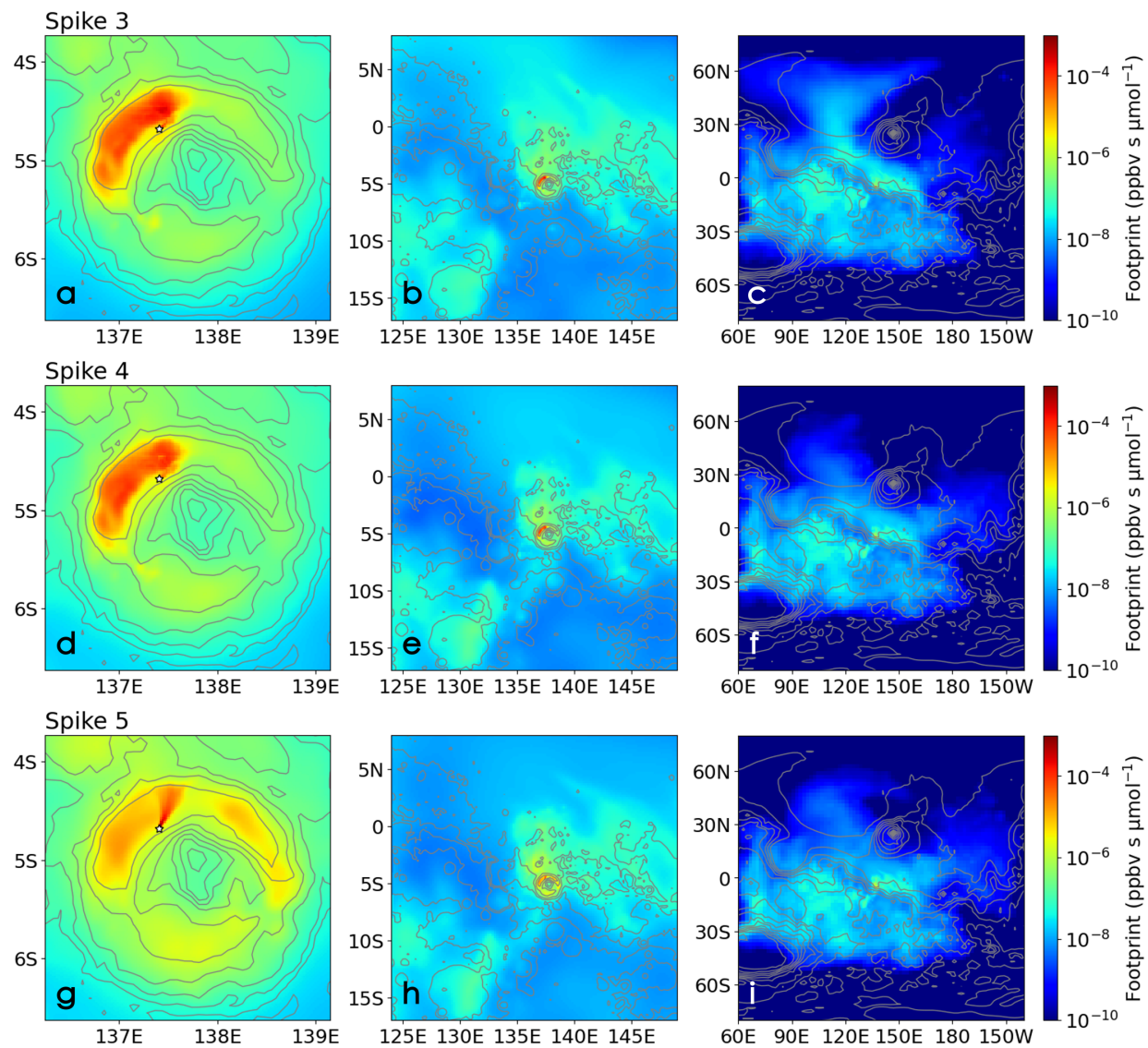


Fig. S5. Same as Fig. 3, but for (a–c) Spike 3, (d–f) Spike 4, (g–i) Spike 5.

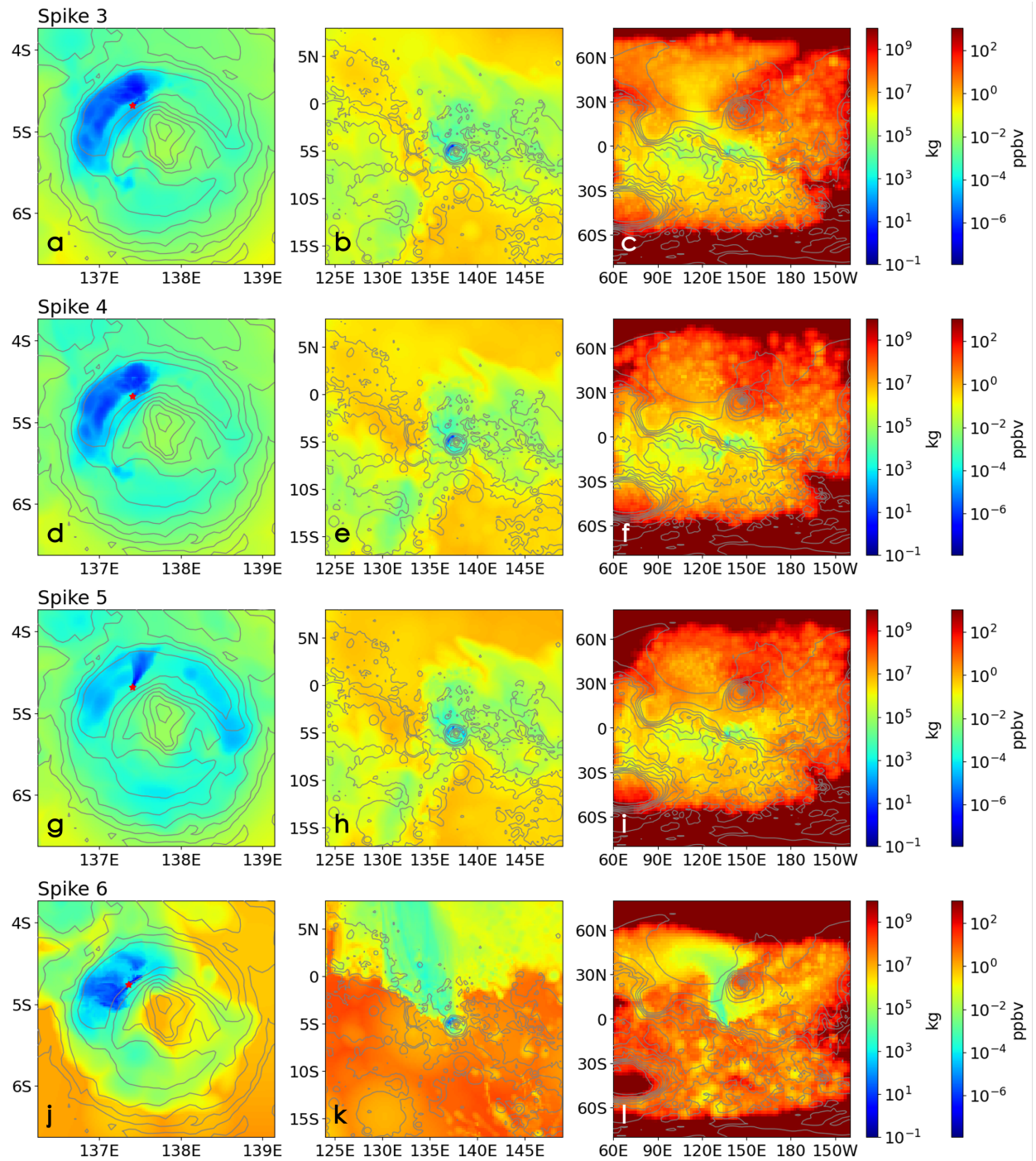


Fig. S6. Same as Fig. 4, but for (a–c) Spike 3, (d–f) Spike 4, (g–i) Spike 5, and (j–l) Spike 6.

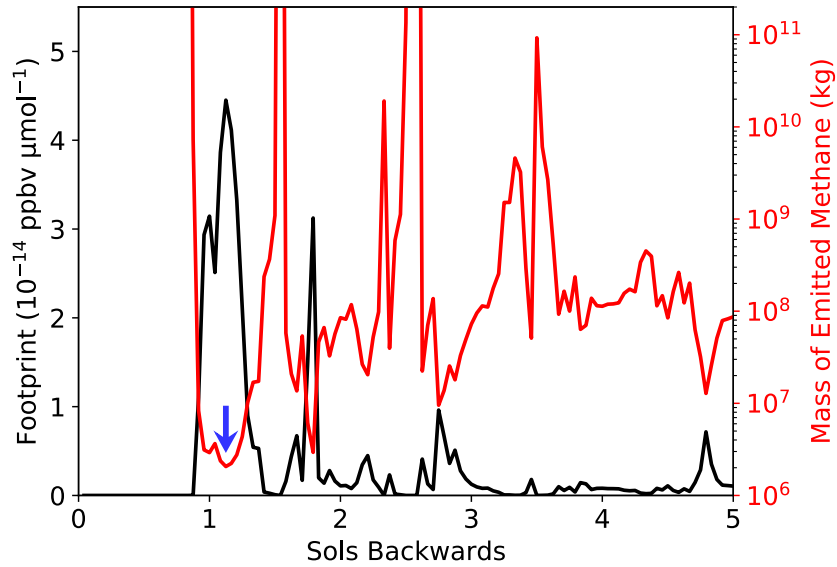


Fig. S7. An example time series of the footprint magnitude for Spike 1 at the center of the “E8” region in Giuranna et al. (2019) (4°S, 144°E). The emission site is about 390 km away

from the *Curiosity* rover. The black curve shows the STILT footprint versus time backwards

with respect to the time of detection. The zero footprint within the first twenty hours means that any emission that takes place at this emission site less than twenty hours before the detection will

not reach the detection site at *Curiosity*. The red curve shows the mass of emitted methane that

can give rise to the methane signal, assuming methane is instantaneously emitted. The blue arrow indicates the moment of maximum influence of the emission site on the methane signal, which

manifests itself as the smallest emitted methane abundance. To produce Spike 1, this emission

site has to emit at least two thousand tons of methane, which is equivalent to 0.23 ppbv global

mean methane concentration. If the emission occurred at a random time within five sols before the detection, this figure shows that in general 10^4 to 10^5 tons of methane needs to be emitted.

The emitted mass for the “E8” region found in Giuranna et al. (2019) is 1170 to 2740 tons, which

is about the same as the lower limit estimated in this study.

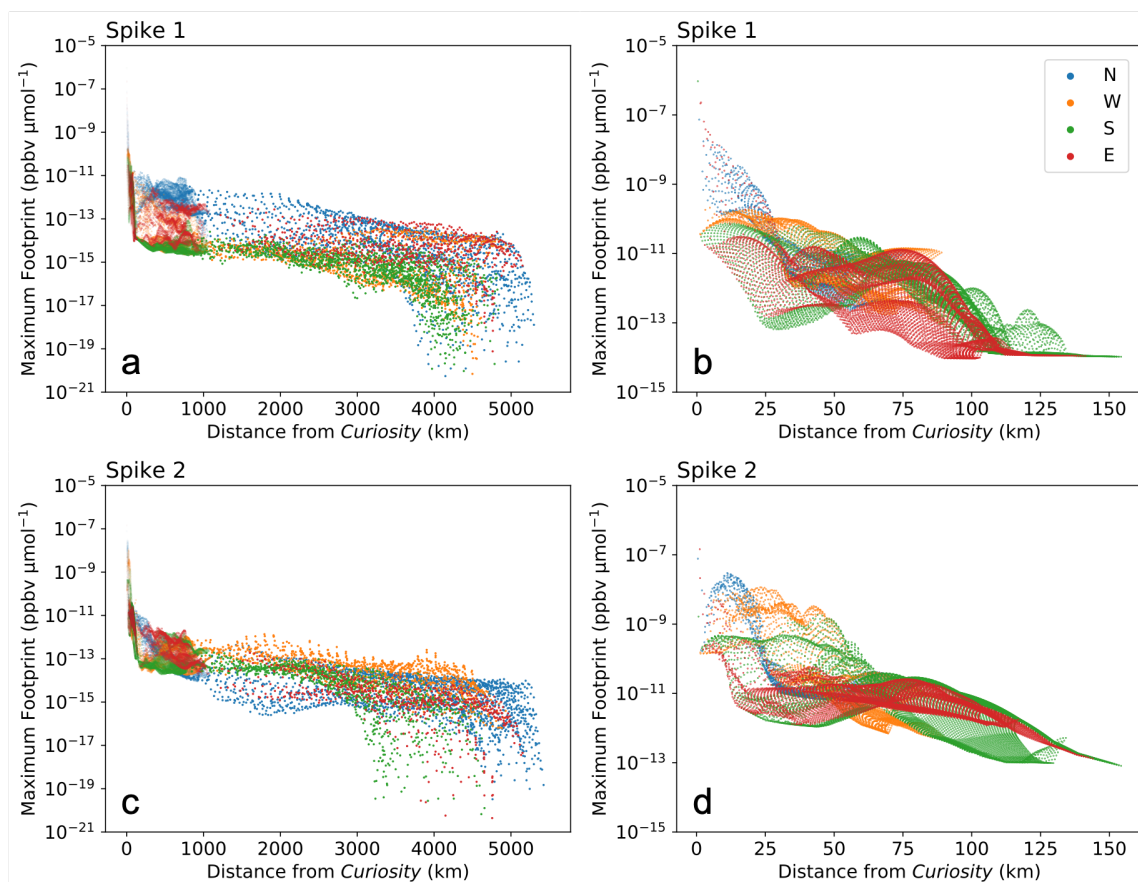


Fig. S8. Decay of STILT footprint with distance. Shown is the maximum STILT footprint (a) and (b) for Spike 1 and (c) and (d) for Spike 2 at every putative emission site around the detector versus the distance between the emission site and the detector. (a) and (c) show all the emission sites in Fig. 3(c). (b) and (d) only show emission sites within and in the vicinity of Gale crater. Blue dots indicate emission sites in the northern quadrant, yellow dots, in the western quadrant, green dots, in the southern quadrant, and red dots, in the eastern quadrant. The drop of footprint magnitude at long distances (> 3000 km) in (a) and (c) is due to an insufficient number of particles that reach these distant places in the STILT simulations. It is found that the maximum footprint decays rapidly with distance while within Gale crater. Outside Gale crater, the decay is slower. This figure demonstrates of the necessity of modeling atmospheric dispersion when one wants to build a linkage between emission fluxes and methane signals, because the linkage strongly depends on the distance between the emission site and the detector.

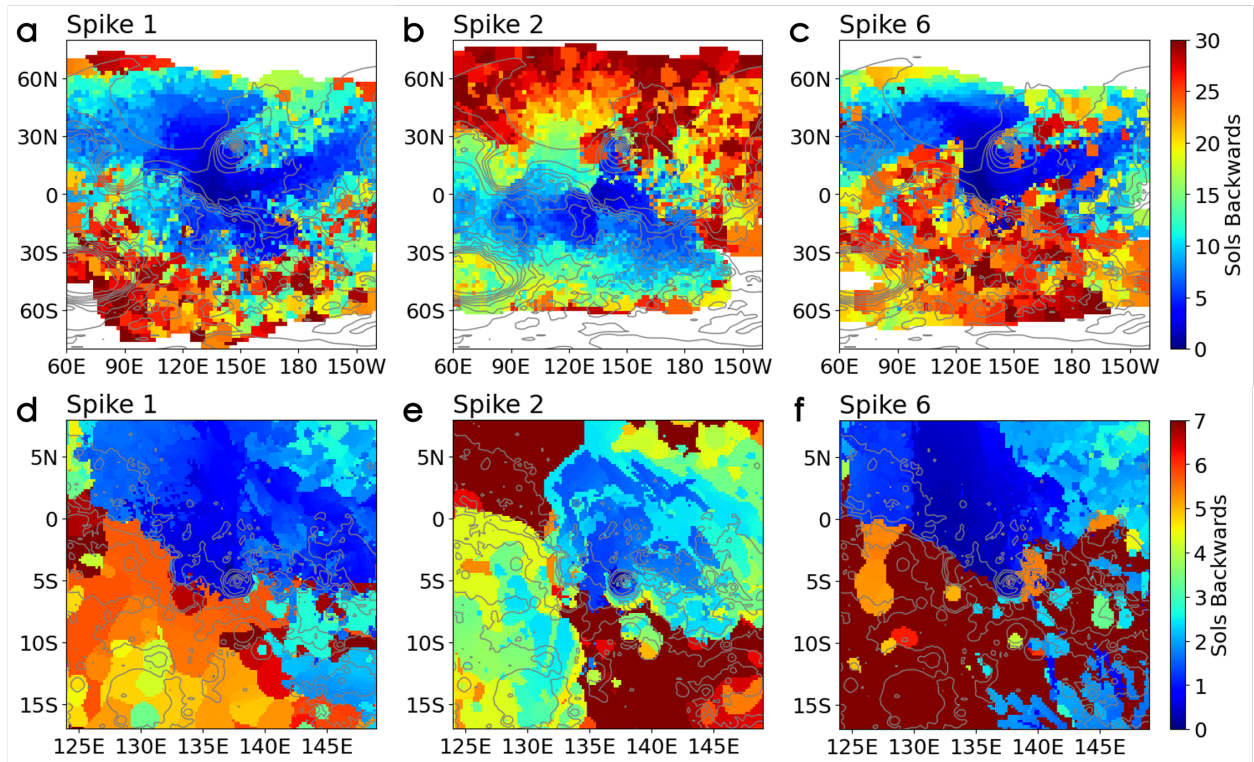


Fig. S9. Time of maximum STILT footprint for (a) and (d) Spike 1, (b) and (e) Spike 2, and (c) and (f) Spike 6 at all emission sites. One can refer to the blue arrow in Fig. S7 for the meaning of “maximum STILT footprint”. This figure shows the transport timescales. (a–c) show the entire domain of the simulation. (d–f) zoom into the vicinity of Gale crater. It takes less than one sol to transport methane signals emitted from anywhere within Gale crater to the *Curiosity* rover. For Spikes 1 and 6, it takes less than one week to transport methane signals emitted from Elysium Planitia, Utopia Planitia, and Amazonis Planitia to the detector, whereas it can take up to a few weeks to more than one month to transport methane signals emitted from the southern highlands to the detector. For Spike 2, it takes about one week to transport methane signals emitted from Hesperia Planum and Terra Cimmeria to the *Curiosity* location, whereas it can take up to a few weeks or longer to transport methane signals emitted from the northern lowlands to the detector. The figures for Spikes 3, 4, and 5 are similar to those for Spike 2.

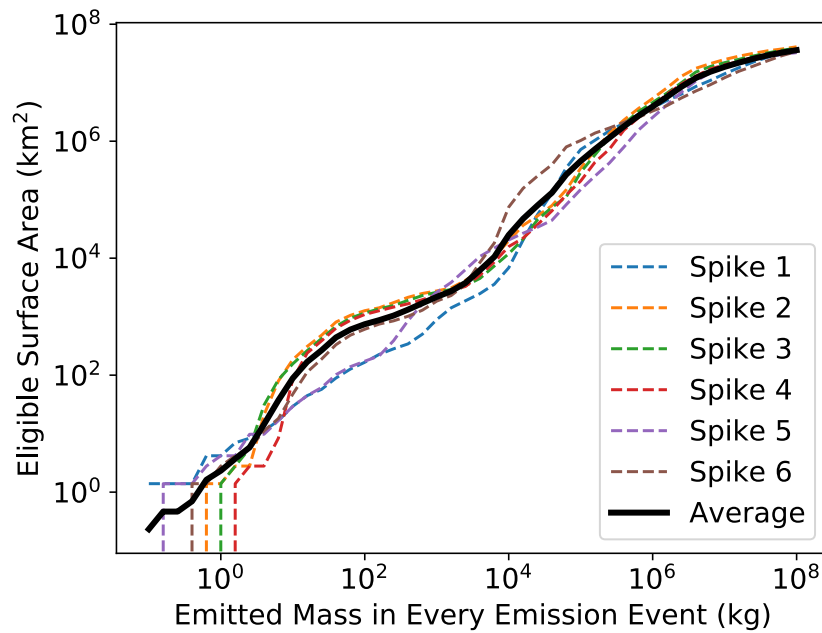


Fig. S10. The maximum area of the emission regions where certain amounts of emitted

methane can produce the observed methane spikes. This figure shows the information in Fig.

4 and Fig. S6 from another perspective. Recalling that TGO reported an upper limit of 0.02 ppbv

5 for the long-term steady-state methane abundance in the atmosphere assuming methane is a long-

lived species, if the lifetime of methane is 330 years as suggested by standard photochemical

models, no more than ~520 kg of methane is replenished in the atmosphere every year on

average. TLS detected six methane spikes during its 4.6 Earth years of operation, meaning that

no fewer than six emission events happened during this period of time (and possibly many

10 more). Should the emission events not significantly perturb the long-term steady state methane

abundance, no more than 400 kg of methane can be emitted by each emission event. This figure

shows that only an area of 1300 km² around the detector (about 7% the total area of Gale crater)

is able to produce an observed methane spike by emitting 400 kg of methane. This quantitatively

demonstrates how lucky we were to send *Curiosity* to the exact place that is very close to an

15 active surface emission site. Alternatively, there must be fast methane removal mechanisms at

work, or either the TLS spikes or the TGO upper limits need to be reevaluated.